

# Yttrium Oxide Upconverting Phosphors. Part 2<sup>†</sup>: Temperature Dependent Upconversion Luminescence Properties of Erbium in Yttrium Oxide

J. Silver,\* M. I. Martinez-Rubio, T. G. Ireland, and R. Withnall\*

Centre for Phosphors and Display Materials, Chemical and Life Sciences, University of Greenwich, London, SE18 6PF, United Kingdom

Received: January 24, 2001; In Final Form: May 24, 2001

Emission bands from  $\text{Er}^{3+}$  ions on  $\text{C}_2$  and  $\text{S}_6$  sites of cubic  $\text{Y}_2\text{O}_3$  have been observed under 632.8 nm excitation. The well-known green hot band in the region of 520–540 nm and a new blue-green hot band in the region of 469–474 nm have been observed from  $\text{Er}^{3+}$  on both sites. These hot bands are assigned to the  $^2\text{H}_{11/2} \rightarrow ^4\text{I}_{15/2}$  and the  $^4\text{F}_{3/2} \rightarrow ^4\text{I}_{15/2}$  transitions, respectively. In addition to observing different thermal behavior for the emissions from  $\text{Er}^{3+}$  ions on different lattice sites due to these transitions, different thermal behavior has also been observed for the  $^4\text{F}_{5/2} \rightarrow ^4\text{I}_{15/2}$ ,  $^4\text{F}_{9/2} \rightarrow ^4\text{I}_{15/2}$ ,  $^4\text{S}_{3/2} \rightarrow ^4\text{I}_{15/2}$ , and  $^4\text{I}_{11/2} \rightarrow ^4\text{I}_{15/2}$  transitions. The  $^4\text{G}_{11/2} \rightarrow ^4\text{I}_{15/2}$ ,  $^2\text{H}_{9/2} \rightarrow ^4\text{I}_{15/2}$ , and  $^4\text{I}_{9/2} \rightarrow ^4\text{I}_{15/2}$  transitions gave rise to bands which were too weak for accurate temperature-dependent studies. Emission arising from the  $^4\text{F}_{7/2} \rightarrow ^4\text{I}_{15/2}$  transition was observed with 514.5 but not 632.8 nm excitation.

## Introduction

Recently, we reported the effect of particle morphology and crystallite size on the upconversion luminescence properties of erbium and ytterbium codoped yttrium oxide phosphors.<sup>1</sup> In the course of that work, the temperature dependence of the  $^2\text{H}_{11/2} \rightarrow ^4\text{I}_{15/2}$  transition was studied, and it was demonstrated that it was made up of two sets of emission bands. The cubic  $\text{Y}_2\text{O}_3$ : $\text{Er}^{3+}$  lattice contains two crystallographic sites in which the  $\text{M}^{3+}$  ions are found (see Figure 1), one has  $\text{C}_2$  symmetry and the other  $\text{S}_6$  symmetry; both sites are six coordinate and are present in the ratio of 3:1.<sup>2–6</sup> The spectra were interpreted to indicate that the  $\text{Er}^{3+}$  ions on the more symmetrical  $\text{S}_6$  site experienced the smaller crystal field (and hence Stark splitting) and that the  $^2\text{H}_{11/2}$  level of the ion on that site was closer to its  $^4\text{S}_{3/2}$  level (as it was still thermally activated at  $-190^\circ\text{C}$ ) than that of the  $\text{Er}^{3+}$  on the  $\text{C}_2$  site. Indeed, the emission spectrum at  $-190^\circ\text{C}$  did not exhibit bands due to a  $^2\text{H}_{11/2} \rightarrow ^4\text{I}_{15/2}$  transition of  $\text{Er}^{3+}$  on the  $\text{C}_2$  site. In this paper, we report the temperature dependence of all the other transitions in the range 405 to 895 nm for cubic  $\text{Y}_2\text{O}_3$ : $\text{Er}^{3+}$ , as seen using 632.8 nm laser excitation for efficient upconversion.

## Experimental Section

**Chemical Preparation.** The chemicals used in this study are yttrium oxide (99.99%, Rhone Poulenc, France), erbium(III) nitrate pentahydrate (99%, Aldrich), urea and nitric acid (BDH AnalaR). The urea homogeneous precipitation method<sup>7–14</sup> was used to prepare spherical  $\text{Y}_2\text{O}_3$ : $\text{Er}^{3+}$  hydroxycarbonate submicrometer phosphor precursor powders. Yttrium nitrate stock solution (56.4 g/L) was prepared by dissolving  $\text{Y}_2\text{O}_3$  in dilute nitric acid until the solution reached a pH of 3. Erbium nitrate (0.02 g) and urea (15.0 g) were dissolved in 500 mL of the  $\text{Y}(\text{NO}_3)_3$  stock solution after it had been diluted 20-fold with de-ionized water. The solution was kept boiling on a hot plate until turbidity was observed, then it was left for 1 h. The precipitates were filtered and washed twice with deionized water.

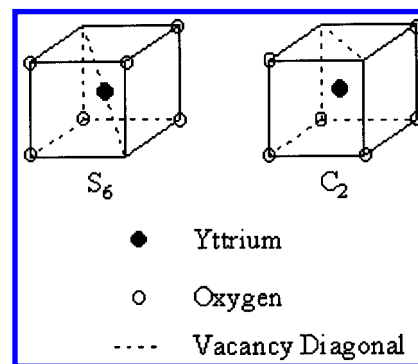


Figure 1. Two  $\text{Y}^{3+}$  crystallographic sites in cubic  $\text{Y}_2\text{O}_3$ .

The precipitates were dried at  $60^\circ\text{C}$  giving soft, white powders which were converted to the oxide by firing at  $980^\circ\text{C}$  in air for 6 h. All the powders consisted of  $\text{Y}_2\text{O}_3$  in the cubic phase as was made evident by X-ray powder diffraction data.<sup>1</sup>

**Characterization of Physical Properties.** The morphologies and the particle sizes of the samples were determined by scanning electron microscope (SEM) (Cambridge Instruments, Stereoscan 90), and TEM using a JEOL JEM-200CX. The average diameter of the spherical particles was estimated to be  $300 \pm 50$  nm from measuring  $\sim 50$  particles per SEM picture.

Luminescence and Raman spectra were obtained using a Labram Raman spectrometer equipped with an 1800 grooves/mm holographic grating, a holographic supernotch filter and a peltier-cooled CCD detector. Samples were excited using a helium–neon laser with an output of 8 mW of power at the sample with the 632.8 nm line, unless an attenuation filter was used. Precise control of sample temperature ( $\pm 0.1^\circ\text{C}$ ) was achieved by means of a Linkam THMS600 temperature programmable heating/cooling microscope stage. For cooling, the THMS stage was used in conjunction with a Linkam LNP cooling system.

Spectral intensities were normalized using the Stokes Raman band at  $375\text{ cm}^{-1}$  of cubic  $\text{Y}_2\text{O}_3$ .

<sup>†</sup> Part 1 of this series is reference 1 of this work.

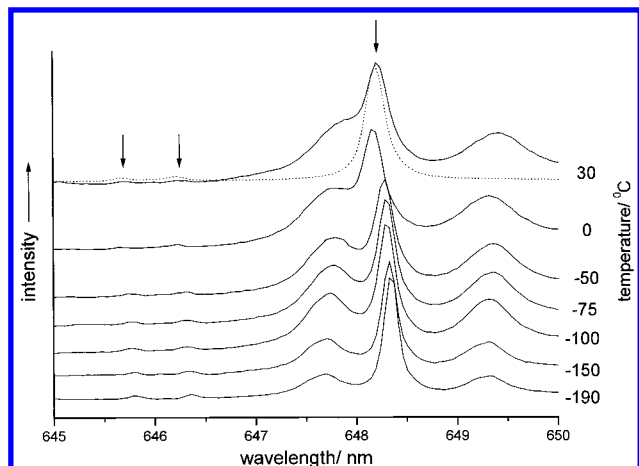


**Figure 2.** Stokes region showing  $\text{Y}_2\text{O}_3$  Raman bands, indicated by arrows. The dotted trace shows the spectrum obtained from pure  $\text{Y}_2\text{O}_3$  at 30 °C. The solid traces show the spectra obtained from  $\text{Y}_2\text{O}_3:\text{Er}^{3+}$  at the indicated temperatures (in °C). Also present are two small emission bands centered at 647.7 and 649.3 nm.

## Results and Discussion

The anti-Stokes and Stokes emission spectra from cubic  $\text{Y}_2\text{O}_3:\text{Er}^{3+}$  were shown in Figures 5 and 6 of our previous work<sup>1</sup> for the ranges 405 to 630 and 635 to 895 nm, respectively. It was demonstrated that the  $^2\text{H}_{11/2} \rightarrow ^4\text{I}_{5/2}$  transition was made up of contributions from the  $\text{Er}^{3+}$  in the  $\text{C}_2$  and  $\text{S}_6$  lattice sites.<sup>1</sup> All the emission band assignments referred to herein are summarized in Figure 7 of ref 1, and the assignments of the present work are given in the final Figure of this article. As the  $\text{S}_6$  lattice site has a higher symmetry, the assumption was made that this would generate the smallest crystal field, and hence, the  $\text{Er}^{3+}$  ions on these sites would experience the smallest Stark splitting (480  $\text{cm}^{-1}$ ) compared to 720  $\text{cm}^{-1}$  on the other  $\text{Er}^{3+}$  site (the  $\text{C}_2$  site). Moreover, the  $^2\text{H}_{11/2} \rightarrow ^4\text{I}_{5/2}$  transition was still thermally active at  $-190$  °C showing the  $^2\text{H}_{11/2}$  level for the  $\text{Er}^{3+}$  on the  $\text{S}_6$  site was closer to its  $^4\text{S}_{3/2}$  level than the  $^2\text{H}_{11/2}$  level on the  $\text{C}_2$  site. The discussion of the thermal behavior of any other emission bands was beyond the scope of that paper but is the subject of this one. It should be stressed that the  $\text{Y}_2\text{O}_3:\text{Er}^{3+}$  Raman band at 375  $\text{cm}^{-1}$  and weaker bands at 315 and 328  $\text{cm}^{-1}$  on the Stokes side (Figure 2) move to higher wavenumber by 2.5  $\text{cm}^{-1}$  on decreasing the temperature from 30 to  $-190$  °C.<sup>1</sup> This is most likely due to a small contraction of the lattice which, however, does not give rise to similar, temperature-dependent shifts of all of the emission bands. The fact that the emission bands do not shift as the temperature decreases (see for instance Figures 3 to 6) is evidence that the crystal field splittings on both the  $\text{C}_2$  and  $\text{S}_6$   $\text{Er}^{3+}$  sites do not change measurably in magnitude or direction, over this temperature range. Figure 3 covers the region 545–562 nm. The emission bands in this region maximize at  $-50$  °C (the intense band at 563.8 nm is saturated and is not shown). These bands are due to the  $^4\text{S}_{3/2} \rightarrow ^4\text{I}_{15/2}$  transitions, and their temperature dependence indicates that two bands, at 549.4 and 550.9 nm (indicated in Figure 3 by arrows), behave differently from the others. These two bands maximize in intensity at  $-190$  °C, and their intensities are approximately one-third of the intensities of the strongest two bands (at 553.8 and 563.8 nm) in this wavelength region. In light of the intensities of these bands and their wavelength positions, they can be assigned to  $\text{Er}^{3+}$  on the  $\text{S}_6$  site. The remaining bands between 545 and 565 nm can be assigned to  $\text{Er}^{3+}$  on the  $\text{C}_2$  site; they all show a temperature dependence which maximizes at  $-50$  °C. The overall temperature depen-

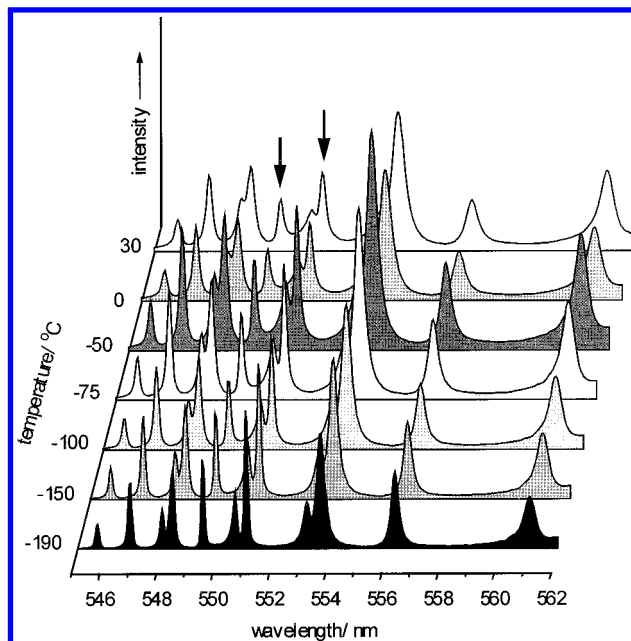


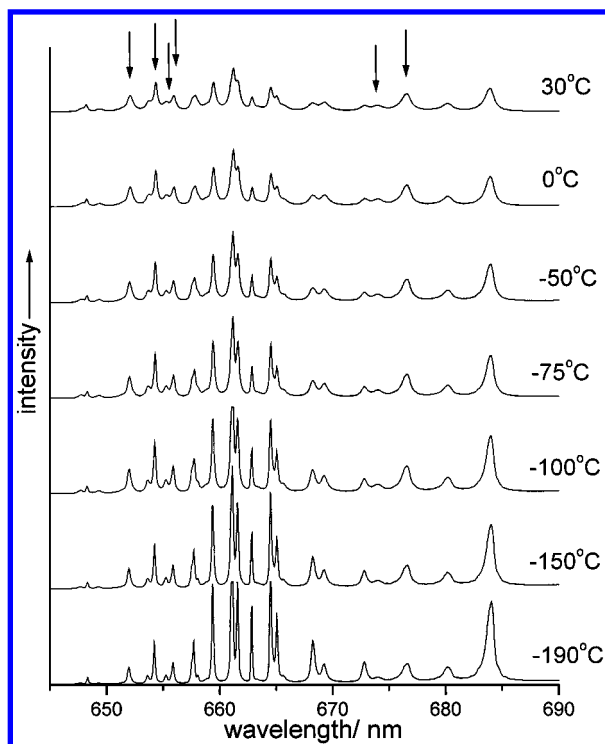
**Figure 3.** Emission bands due to the  $^4\text{S}_{3/2} \rightarrow ^4\text{I}_{15/2}$  transitions of  $\text{Er}^{3+}$  on the  $\text{C}_2$  and  $\text{S}_6$  sites in  $\text{Y}_2\text{O}_3$ . The bands due to  $\text{Er}^{3+}$  on the  $\text{C}_2$  site maximize at  $-50$  °C, whereas the two bands (indicated by arrows) due to  $\text{Er}^{3+}$  on the  $\text{S}_6$  site maximize at  $-190$  °C.

dence of these bands seems to be anomalous (see Figure 3); however, the intensities of the bands due to the other transitions showed steady, temperature-dependent trends, as expected. We therefore tentatively suggest that the behavior exhibited by the  $^4\text{S}_{3/2} \rightarrow ^4\text{I}_{15/2}$  transition appears to indicate that the  $^4\text{S}_{3/2}$  level may also be populated by an additional mechanism (which is most likely to be cross-relaxation).

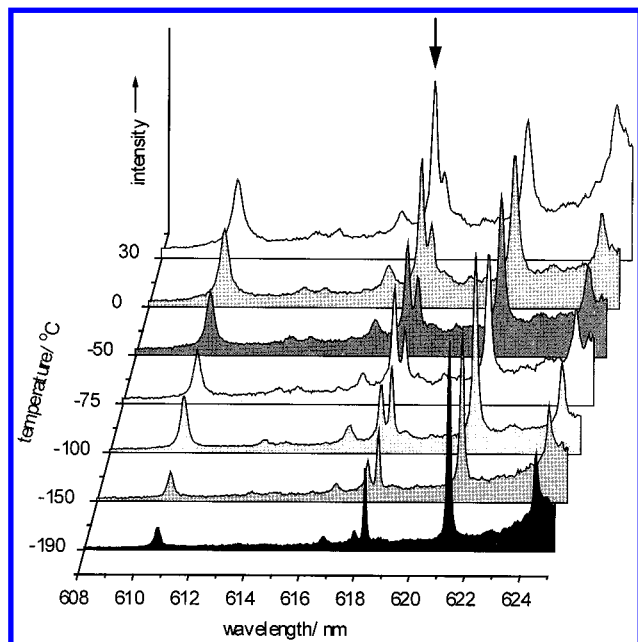
The assignment of the bands to  $\text{Er}^{3+}$  ions on the  $\text{C}_2$  and  $\text{S}_6$  sites is in keeping with the relative intensities. In addition, it can be seen that the  $\text{Er}^{3+}$  ion on the  $\text{S}_6$  site has a smaller  $^2\text{H}_{11/2} - ^4\text{S}_{3/2}$  energy gap than the  $\text{Er}^{3+}$  on the  $\text{C}_2$  site by taking the difference in wavelength between the maximum intensity bands of the  $^4\text{S}_{3/2} \rightarrow ^4\text{I}_{15/2}$  and  $^2\text{H}_{11/2} \rightarrow ^4\text{I}_{15/2}$  transitions for both sites.

Figure 4 covers the region 650–700 nm (on the Stokes side). The bands in the range 647.8 to 684 nm are due to the  $^4\text{F}_{9/2} \rightarrow ^4\text{I}_{15/2}$  emission. The temperature dependencies of these bands are clearly different. Those not marked by arrows maximize at  $-190$  °C and span the range 657.8 to 684 nm (26.2 nm in total). These bands include many of the most intense bands in this region, and hence, these bands are assigned to the  $\text{Er}^{3+}$  ions on the  $\text{C}_2$  lattice site. The other bands, which are marked by arrows in Figure 4 and maximize at  $-100$  °C, can be assigned to the  $\text{Er}^{3+}$  ions on the  $\text{S}_6$  lattice site. It is noteworthy that, at any given temperature, the most intense band of  $\text{Er}^{3+}$  on the  $\text{S}_6$  site is only approximately one-third as intense as its counterpart of  $\text{Er}^{3+}$  on the  $\text{C}_2$  site. It should be noted that the intense band at 661.3 nm is saturated but most probably also maximizes at  $-190$  °C.

Three weak bands at 754.1, 765.6, and 770.7 nm were not ascribed previously to any main transition,<sup>1</sup> and their independent temperature dependence has not thrown light on their origin. The bands due to the  $^4\text{I}_{9/2} \rightarrow ^4\text{I}_{15/2}$  transition in the 785 to 830 nm region were very weak, and because of the background changes, were very difficult to ascribe further to particular lattice sites. The bands between 845 and 882 nm are due to the  $^4\text{I}_{11/2} \rightarrow ^4\text{I}_{15/2}$  transition; these can be divided into two groups which are assigned to the  $\text{Er}^{3+}$  ion on the  $\text{C}_2$  and  $\text{S}_6$  lattice sites. The bands at 853.1, 855.5, 858.8, 859.3, 866.9,



**Figure 4.** Emission bands due to the  $^4F_{9/2} \rightarrow ^4I_{15/2}$  transitions of  $\text{Er}^{3+}$  on the  $\text{C}_2$  and  $\text{S}_6$  sites in  $\text{Y}_2\text{O}_3$ . The bands not marked with arrows which maximize at  $-190^\circ\text{C}$  are due to  $\text{Er}^{3+}$  on the  $\text{C}_2$  site, whereas the six bands indicated by arrows are due to  $\text{Er}^{3+}$  on the  $\text{S}_6$  site and maximize at  $-100^\circ\text{C}$ .



**Figure 5.** Emission bands of  $\text{Er}^{3+}$  in  $\text{Y}_2\text{O}_3$  in the 610–625 nm region. The arrow marks the strong Raman band of  $\text{Y}_2\text{O}_3$  on the anti-Stokes side.

877.8, and 879.8 nm (range 853.1 to 879.8 nm = 26.7 nm) all maximize at  $-190^\circ\text{C}$ , whereas those at 846.9, 849.2, 871.2, and 873.2 nm (range 26.3 nm) all maximize around  $-100^\circ\text{C}$ . The bands in the slightly larger range, which maximize at  $-190^\circ\text{C}$ , are ascribed to the  $\text{Er}^{3+}$  ion on the  $\text{C}_2$  lattice site, and the bands in the slightly smaller range, maximizing at  $-100^\circ\text{C}$ , are ascribed to the  $\text{Er}^{3+}$  ion on the  $\text{S}_6$  site, on the basis of their relative intensities.

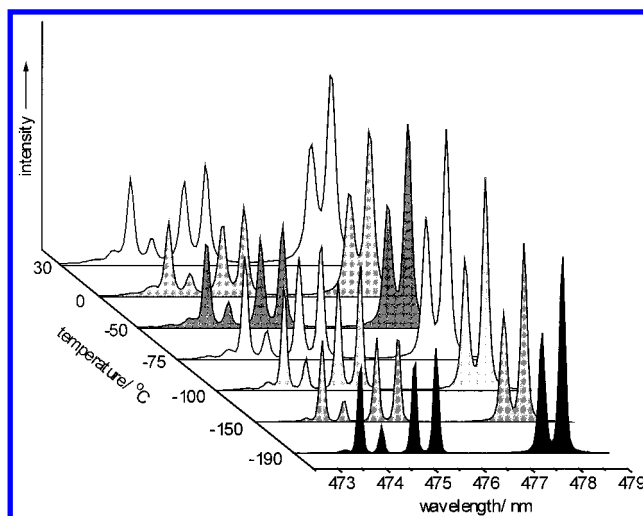


**Figure 6.** Emission bands of  $\text{Er}^{3+}$  in  $\text{Y}_2\text{O}_3$  in the 472.5–479.0 nm region.

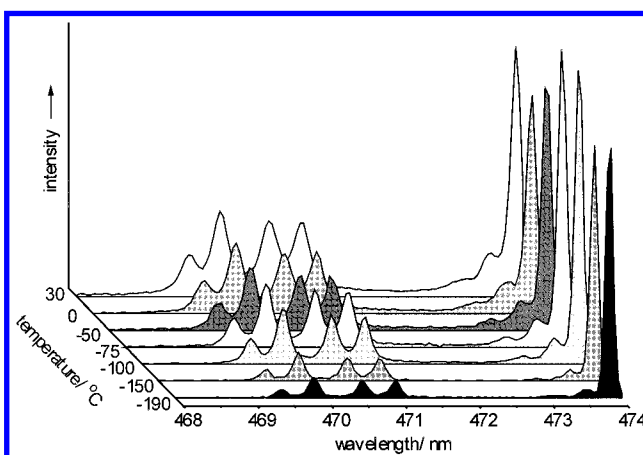


**Figure 7.** Emission bands of  $\text{Er}^{3+}$  in  $\text{Y}_2\text{O}_3$  in the 468.0–474.0 nm region. Two groups of hot bands are seen; the first is a group of four between 469.0 and 471.5 nm and the second is a group of two between 473.2 and 473.6 nm.

The  $\text{Y}_2\text{O}_3$  Raman band on the anti-Stokes side (Figure 5) at  $375\text{ cm}^{-1}$  loses intensity with temperature, as expected, as it originates from the  $\nu = 1$  excited vibrational level which is thermally populated. The emission bands in this region show varied temperature dependencies. The bands at 610.7, 613.6, and 616.7 nm maximize at  $-100^\circ\text{C}$ , whereas the bands at 618.2, 621.2, and 624.4 nm maximize at  $-190^\circ\text{C}$ . These bands were tentatively attributed to transitions between excited states<sup>1</sup> and, although it can be seen from their temperature behavior that they originate from  $\text{Er}^{3+}$  on the two different lattice sites, further assignment is not possible.

It was previously suggested that the bands between 468 and 477 nm were due to the  $^4F_{7/2} \rightarrow ^4I_{15/2}$  transition,<sup>1</sup> however examination of Figures 6 and 7 indicates that the true picture is clearly more complex. The bands at 473.8, 474.2, 475.1, and 476.0 nm (see Figure 6) maximize at  $-100^\circ\text{C}$ , the two bands at 478.0 and 478.5 maximize at  $-75^\circ\text{C}$ , but the four bands between 469 and 471.5 nm in Figure 7 behave like hot bands, losing intensity progressively from room temperature downward. In addition, the two small bands at 473.2 and 473.6 nm (see Figure 7) also show behavior characteristic of hot bands. It is now apparent that the four bands between 473.8 and 476.0 nm are due to the  $^4F_{5/2} \rightarrow ^4I_{15/2}$  transition of the  $\text{Er}^{3+}$  on the  $\text{S}_6$  lattice site, and that the two bands at 478.0 and 478.5 nm are due to the  $^4F_{5/2} \rightarrow ^4I_{15/2}$  transition of  $\text{Er}^{3+}$  on the  $\text{C}_2$  lattice site

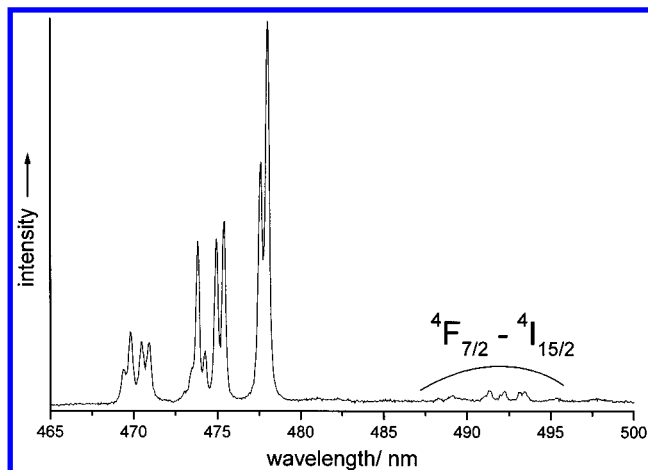


**Figure 8.** Emission bands of  $\text{Er}^{3+}$  in  $\text{Y}_2\text{O}_3$  in the 465–500 nm region under 514.5 nm excitation.

(assigned on the basis of relative intensities). The new hot band must therefore be due to the  ${}^4\text{F}_{3/2} \rightarrow {}^4\text{I}_{15/2}$  transition, and the bands between 469.0 and 471.5 nm are from  $\text{Er}^{3+}$  on the  $\text{S}_6$  site, whereas the two at 473.2 and 473.6 nm originate from  $\text{Er}^{3+}$  on the  $\text{C}_2$  site. The  ${}^4\text{F}_{7/2} \rightarrow {}^4\text{I}_{15/2}$  transition is in fact not observed in these experiments using 632.8 nm excitation, and this is presumably due to nonradiative decay, in keeping with assignments for other systems.<sup>15,16</sup> However, it was possible to observe very weak bands in the expected region for a  ${}^4\text{F}_{7/2} \rightarrow {}^4\text{I}_{15/2}$  transition using 514.5 nm excitation from an argon ion laser. Eight emission lines between 488.3 and 497.8 nm were observed (see Figure 8), but they were too weak to merit an in depth temperature study for their assignment to  $\text{Er}^{3+}$  on a specific lattice site.

The two emission lines at 405 and 409 nm (due to the  ${}^2\text{H}_{9/2} \rightarrow {}^4\text{I}_{15/2}$  transition) and the group between 452 and 465 nm, which are now assigned to the  ${}^4\text{G}_{11/2} \rightarrow {}^4\text{I}_{15/2}$  transition, were so weak that their temperature dependent changes were too small to be studied accurately.

Finally, it is possible to predict the relative populations of the  ${}^4\text{S}_{3/2}$  and  ${}^2\text{H}_{11/2}$  levels using a three level model comprising of the former (level 2), the latter (level 3), and the  ${}^4\text{I}_{15/2}$  ground level. This can be achieved by making use of the following equation<sup>15,17</sup>

$$\frac{I_3}{I_2} = A \exp\left(-\frac{E_{32}}{kT}\right)$$

where  $I_3$  and  $I_2$  are the integrated emission intensities of the  ${}^2\text{H}_{11/2} \rightarrow {}^4\text{I}_{15/2}$  and  ${}^4\text{S}_{3/2} \rightarrow {}^4\text{I}_{15/2}$  transitions of the  $\text{Er}^{3+}$  ion, respectively,  $E_{32}$  is the energy gap between the  ${}^2\text{H}_{11/2}$  and  ${}^4\text{S}_{3/2}$  levels, and  $k$  is Boltzmann's constant. The preexponential factor,  $A$ , is given by the following equation

$$A = \frac{W_{R3}g_3hv_3}{W_{R2}g_2hv_2}$$

where  $W_{R3}$  and  $W_{R2}$  are the radiative probabilities of these two transitions,  $g_3$  and  $g_2$  are the  $(2J + 1)$  degeneracies of levels 3 and 2, respectively, and  $hv_3$  and  $hv_2$  are the photon energies of the respective transitions from levels 3 and 2 to level 1.

Such an analysis for the  $\text{C}_2$  and  $\text{S}_6$  sites yields the straight line plots in Figure 9. That for the  $\text{C}_2$  site gives an  $E_{32}$  value of 628  $\text{cm}^{-1}$ . It is apparent from Figure 9 that the value of  $I_3/I_2$  is  $\sim 0.04$  at  $-100^\circ\text{C}$ . This means that the  ${}^2\text{H}_{11/2} \rightarrow {}^4\text{I}_{15/2}$  transition would not be observed at  $-190^\circ\text{C}$ . The  $A$  parameter for this

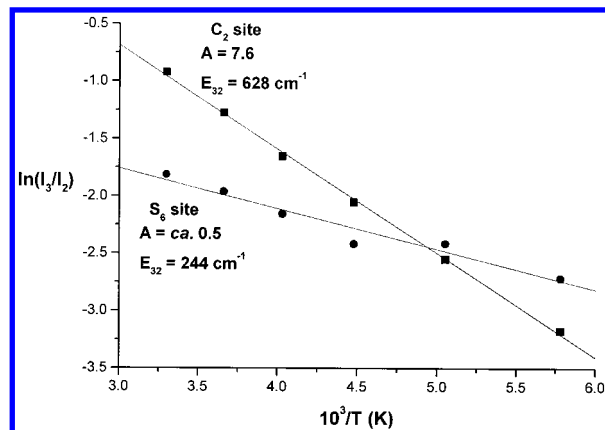


**Figure 9.** Logarithm of the ratios of the integrated intensities of the  ${}^2\text{H}_{11/2} \rightarrow {}^4\text{I}_{15/2}$  and  ${}^4\text{S}_{3/2} \rightarrow {}^4\text{I}_{15/2}$  transitions as a function of inverse absolute temperature ( $10^3/T$ ) for the  $\text{C}_2$  and  $\text{S}_6$  sites.

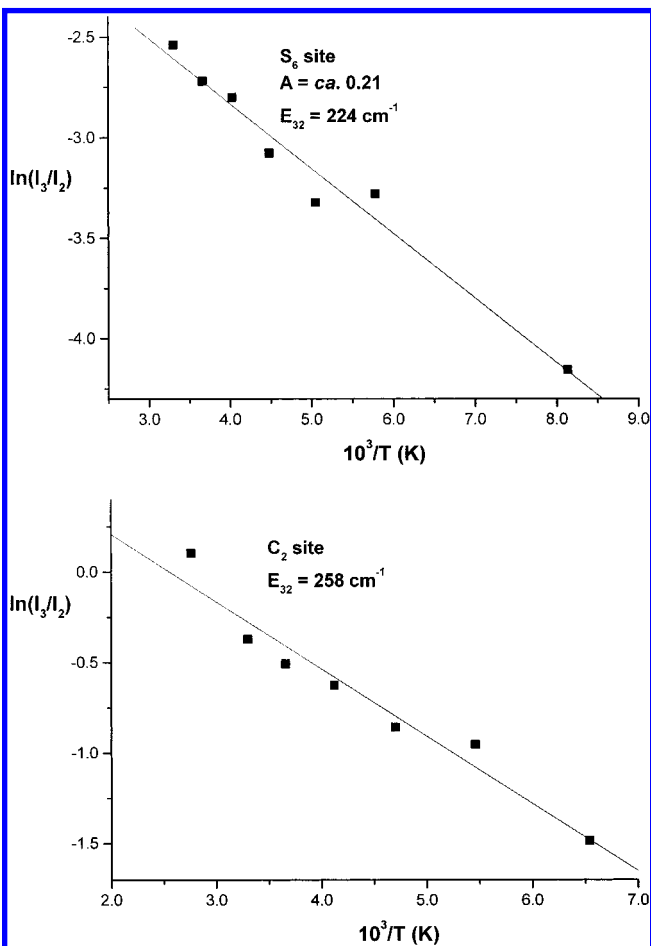


**Figure 10.** (a) Logarithm of the ratio of the integrated intensities of the  ${}^4\text{F}_{3/2} \rightarrow {}^4\text{I}_{15/2}$  and  ${}^4\text{F}_{5/2} \rightarrow {}^4\text{I}_{15/2}$  transitions as a function of inverse absolute temperature ( $10^3/T$ ) for the  $\text{S}_6$  site. (b) Logarithm of the ratio of the peak heights of the  ${}^4\text{F}_{3/2} \rightarrow {}^4\text{I}_{15/2}$  and  ${}^4\text{F}_{5/2} \rightarrow {}^4\text{I}_{15/2}$  transitions as a function of inverse absolute temperature ( $10^3/T$ ) for the  $\text{C}_2$  site.

site is 7.6 which would suggest that the radiative transition probability,  $W_{R3}$ , is greater than  $W_{R2}$ . For the  $\text{S}_6$  site, the value of  $E_{32}$  was found to be 244  $\text{cm}^{-1}$ , in keeping with the fact that emission lines due to this transition are still seen at  $-190^\circ\text{C}$ . The  $A$  parameter for the  $\text{S}_6$  site is ca. 0.50 which can only be interpreted to mean that  $W_{R2}$  is greater than  $W_{R3}$  for this site.

This same theory can of course be applied to the additional hot band which has been observed in the 470 nm region and assigned to the  ${}^4\text{F}_{3/2} \rightarrow {}^4\text{I}_{15/2}$  transition. Such an analysis gives



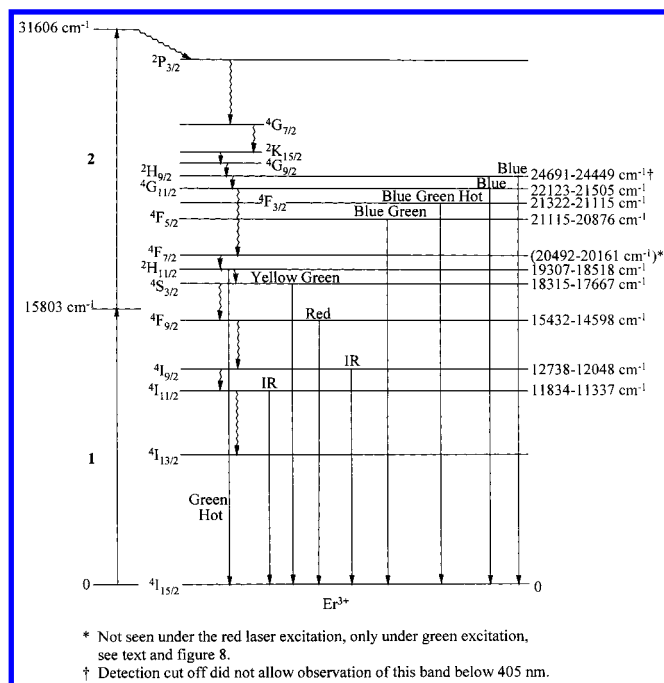


**Figure 11.** Schematic energy level diagram for  $\text{Er}^{3+}$  ions on the two different sites of cubic  $\text{Y}_2\text{O}_3$  and some proposed excitation and emission processes.

a  $^4\text{F}_{3/2}$ – $^4\text{F}_{5/2}$  energy gap for the  $\text{S}_6$  site of  $224\text{ cm}^{-1}$  in keeping with the observation of the band at  $-190^\circ\text{C}$  (see Figure 10a). The  $A$  parameter for the  $\text{S}_6$  site is ca. 0.21 which can only be interpreted to mean that  $W_{R2}$  is greater than  $W_{R3}$  for this site. However, for the  $\text{C}_2$  site, the integrated intensities of the bands due to the  $^4\text{F}_{3/2} \rightarrow ^4\text{I}_{15/2}$  transition were not used, because the bands were overlapped by neighbors. Instead, their peak heights were plotted (see Figure 10b). The value for the  $^4\text{F}_{3/2}$ – $^4\text{F}_{5/2}$  energy gap was found to be  $258\text{ cm}^{-1}$  for this site; this is consistent with the presence of the band at  $-190^\circ\text{C}$ . As the integrated intensities were not used, no reliable  $A$  parameter could be obtained for this site.

## Conclusions

In addition to our previous findings<sup>1</sup> that the two  $\text{Er}^{3+}$  sites in cubic  $\text{Y}_2\text{O}_3:\text{Er}^{3+}$  give rise to  $^2\text{H}_{11/2} \rightarrow ^4\text{I}_{15/2}$  transitions ('hot bands') that show different thermal behavior (due to the  $\text{Er}^{3+}$  ions experiencing different Stark splittings), we have now found evidence that these  $\text{Er}^{3+}$  ions generate other emission bands that also manifest different thermal behavior. The  $^4\text{F}_{3/2} \rightarrow ^4\text{I}_{15/2}$ ,  $^4\text{F}_{5/2} \rightarrow ^4\text{I}_{15/2}$ ,  $^4\text{F}_{9/2} \rightarrow ^4\text{I}_{15/2}$ ,  $^4\text{S}_{3/2} \rightarrow ^4\text{I}_{15/2}$ , and  $^4\text{I}_{11/2} \rightarrow ^4\text{I}_{15/2}$  transitions all manifest different thermal behavior for the  $\text{Er}^{3+}$  ions in the

$\text{C}_2$  lattice sites compared to those in the  $\text{S}_6$  lattice sites. The  $^4\text{G}_{11/2} \rightarrow ^4\text{I}_{15/2}$ ,  $^2\text{H}_{9/2} \rightarrow ^4\text{I}_{15/2}$ , and  $^4\text{I}_{9/2} \rightarrow ^4\text{I}_{15/2}$  transitions gave rise to bands which were too weak for accurate temperature dependency studies. Emission arising from the  $^4\text{F}_{7/2} \rightarrow ^4\text{I}_{15/2}$  transition was observed with 514.5 but not 632.8 nm excitation.

Evidence for new hot bands at 469.0 to 471.5 nm and 473.2 and 473.6 nm was found; these are assigned to the  $^4\text{F}_{3/2}$ – $^4\text{I}_{15/2}$  transition of the  $\text{S}_6$  and  $\text{C}_2$  sites, respectively.

We are now able to construct Figure 11 which is a schematic energy level diagram for  $\text{Er}^{3+}$  ions on the  $\text{C}_2$  and  $\text{S}_6$  sites of  $\text{Y}_2\text{O}_3$ . The energy levels from the  $^4\text{I}_{15/2}$  ground state up to the  $^2\text{H}_{11/2}$  state are assigned as in Figure 7 of ref 1. However the next highest level, the  $^4\text{F}_{7/2}$  level, is now located at  $20\,492$ – $20\,161\text{ cm}^{-1}$ , as an emission has now been observed under 514.5 but not 632.8 nm excitation. The  $^4\text{F}_{5/2}$  level is now located in the  $21\,115$ – $20\,876\text{ cm}^{-1}$  range and the  $^4\text{F}_{3/2}$  level, which was previously unassigned, is at  $21\,322$ – $21\,115\text{ cm}^{-1}$ . The emission from the latter level down to the ground state gives rise to the new hot bands. The blue emission at  $22\,123$ – $21\,505\text{ cm}^{-1}$  can now be assigned to a  $^4\text{G}_{11/2} \rightarrow ^4\text{I}_{15/2}$  transition in keeping with the calculations of Carnall et al. for the free  $\text{Er}^{3+}$  ion,<sup>18</sup> and contrary to both our earlier assignment<sup>1</sup> and that of Xu et al.<sup>15</sup>

**Acknowledgment.** We express our gratitude to the EPSRC (Grant Nos. GR/L85176 and GR/N28535) and also thank Prof. F. Auzel for useful discussions.

## References and Notes

- (1) Silver, J.; Martinez-Rubio, M. I.; Ireland, T. G.; Fern, G. R.; Withnall, R. J. *Phys. Chem. B* **2001**, *105*, 948.
- (2) Paton, M. G.; Maslem, E. N. *Acta Crystallogr.* **1965**, *19*, 307.
- (3) Faucher, M. *Acta Crystallogr. B* **1980**, *36*, 3209.
- (4) Ishibashi, H.; Shimamoto, K.; Nakahigashi, K. *J. Phys. Chem. Solid* **1994**, *9*, 809.
- (5) Mitric, M.; Antic, B.; Balanda, M.; Rodic, D.; Napijalo, M. L. *J. Phys. Condens. Matter* **1997**, *9*, 4103.
- (6) Forest, H.; Ban, G. *J. Electrochem. Soc.* **1969**, *116*, 474.
- (7) Akinc, M.; Sordellet, D. *J. Colloid Interface Sci.* **1998**, *122*(1), 47.
- (8) Milosevic, O.; Jordovic, B.; Uskokovic, D. *Mater. Lett.* **1994**, *19*, 165.
- (9) Kim, M. J.; Matijevic, E. *J. Mater. Res.* **1991**, *6*(4), 840.
- (10) Giesche, H.; Matijevic, E. *J. Mater. Res.* **1994**, *9*(2), 436.
- (11) Nishisu, Y.; Kobayashi, M. U.S. Patent 5,413,736; 1995.
- (12) Pei, Y.; Liu, X. *Chin. J. Lumin.* **1996**, *17*(1), 5.
- (13) Jiang, Y. D.; Wang, Z. L.; Zhang, F.; Paris, H. G.; Summers, C. J. *J. Mater. Res.* **1998**, *13*, 2950.
- (14) Vecht, A.; Gibbons, C.; Davies, D.; Jing, X.; Marsh, P.; Ireland, T. G.; Silver, J.; Newport, A. *J. Vacuum Sci. Technol. B* **1999**, *17*, 750.
- (15) Xu, W.; Dai, S.; Toth, L. M.; Del. Cul, G. D.; Peterson, J. R. *J. Phys. Chem.* **1995**, *99*, 4447.
- (16) Yeh, D. C.; Sibley, W. A.; Suscavage, M.; Drexhage, M. G. *Appl. Phys.* **1987**, *62*(1), 266.
- (17) Shinn, M. D.; Sibley, W. A.; Drexhage, M. G.; Brown, R. N. *Phys. Rev. B* **1983**, *27*, 6635.
- (18) Carnall, W. T.; Goodman, G. L.; Rajnak, K.; Rana, R. S. *J. Chem. Phys.* **1989**, *7*, 3443.